Adaptive phase field modelling of crack propagation in orthotropic functionally graded materials

Hirshikesh [a], Emilio Martínez-Pañeda [b], Sundararajan Natarajan [a, *]

[a] Department of Mechanical Engineering, Indian Institute of Technology Madras, Chennai, 600036, India
[b] Department of Civil and Environmental Engineering, Imperial College London, London, SW7 2AZ, UK

A B S T R A C T

In this work, we extend the recently proposed adaptive phase field method to model fracture in orthotropic functionally graded materials (FGMs). A recovery type error indicator combined with quadtree decomposition is employed for adaptive mesh refinement. The proposed approach is capable of capturing the fracture process with a localized mesh refinement that provides notable gains in computational efficiency. The implementation is validated against experimental data and other numerical experiments on orthotropic materials with different material orientations. The results reveal an increase in the stiffness and the maximum force with increasing material orientation angle. The study is then extended to the analysis of orthotropic FGMs. It is observed that, if the gradation in fracture properties is neglected, the material gradient plays a secondary role, with the fracture behaviour being dominated by the orthotropy of the material. However, when the toughness increases along the crack propagation path, a substantial gain in fracture resistance is observed.

1. Introduction

Functionally graded materials (FGMs) are a special class of composites with spatially varying microstructure - volume fractions of the constituent elements. These characteristics of FGMs allow the designer to develop *ad hoc* microstructures for specific, non-uniform service conditions. In addition, the continuous variation of material properties alleviates weak junctions within the system (for example in layered materials), i.e., avoiding the bi-material interface, which could be a potential site for crack nucleation. The potential advantages in using the FGMs include: (a) enhanced thermal and fracture resistance [1,2], (b) reduced residual stresses [3], and (c) the smoothening of interfaces [4,5]. Ceramic-based FGMs enjoy great popularity [6]. However, these materials exhibit brittle fracture and complex fracture behaviour [7], particularly when a preferential direction of orthotropy develops. The preferential direction of orthotropy can arise due to the

manufacturing process utilized for the synthesis. This is, for example, the case in FGMs manufactured with plasma spray techniques or electron beam physical vapor deposition. In the former, the outcome is a material with a lamellar structure with higher stiffness and weak cleavage planes parallel to the boundary. In FGMs manufactured via electron beam physical vapor deposition one observes a columnar structure, a higher stiffness in the thickness direction and weak fracture planes perpendicular to the boundary [8,9].

Several numerical techniques have been proposed in the literature to analyse the fracture processes in orthotropic FGMs [8,10–14]. The vast majority of the works are based on discrete approaches; for example, the conventional finite element with displacement correlation technique (DCT) [15], the extended finite element method (XFEM) [8,10,11,14], and the scaled boundary finite element method (SBFEM) [12,13]. However, predicting crack initiation and subsequent crack growth requires an *ad hoc* criterion, with crack trajectories being sensitive to this choice [16]. Variational approaches based on energy minimization constitute a promising tool to overcome this limitation [17,18]. Specifically, the phase field method (PFM) has proven to be efficient technique in modelling brittle fracture [19–21], ductile damage [22,23], dynamic fracture [24], fracture properties prediction of

* Corresponding author. Department of Mechanical Engineering, Indian Institute of Technology Madras, Chennai, 600036, India.
E-mail addresses: mail@empaneda.com (E. Martínez-Pañeda), snatarajan@iitm.ac.in, sundararajan.natarajan@gmail.com (S. Natarajan).
Peer review under responsibility of China Ordnance Society

nanocomposites [25], fiber cracking and composites delamination [26–28], plates and shells [29,30] and hydrogen embrittlement [31,32], among other phenomena. Recently, the success of phase field fracture methods has been extended to modelling cracking in isotropic FGMs by Hirshikesh et al. [33]. Here, we extend the framework to deal with orthotropic FGMs and include an adaptive mesh refinement strategy to boost computational efficiency.

Although, the PFM has shown advantages over discrete approaches, the finite element discretization requires resolving the length scale parameter as ℓ_o. In brittle materials, ℓ_o can be very small and the discrete crack in linear elastic fracture mechanics is recovered for the limiting case of $\ell_o \rightarrow 0$. The need to resolve this region of high gradients creates a computational burden. Local refinement techniques can reduce the computational cost; however, this requires the crack path to be known a priori, which is often not the case. An alternative is to use adaptive refinement algorithms based on error indicators. Several strategies have been proposed [34–39], being most of them based on post-error estimation such as goal-oriented, recovery, and residual. For example, Areias et al. [40,41] presented an adaptive mesh refinement strategy that combines the staggered algorithm with the screened Poisson equation. Goswami et al. [42] proposed an adaptive fourth-order phase field model based isogeometric analysis (IGA). Recently, Samaniego et al. [43] solved the phase-field equations via machine learning approach. In this paper, we aim to extend the recently developed adaptive PFM by Hirshikesh et al. [37] to model fracture in orthotropic FGMs. The adaptive PFM is based on the combination of quadtree decomposition and recovery based error indicators, allowing for an automatic tracking of the crack trajectory and local domain discretization. The hanging nodes that arise due to the quadtree decomposition are treated within the framework of the polygonal finite element method (PFEM) with mean - value coordinate basis function.

The rest of the paper is organized as follows. Section 2 presents the governing equations for the PFM and the corresponding weak form. The adaptive refinement strategy based on the quadtree decomposition and recovery based error indicator is presented in Section 3. The applicability of the adaptive refinement strategy for the fracture in orthotropic FGM is shown in Section 4. Concluding remarks end the manuscript.

2. A phase field fracture formulation for orthotropic FGMs

Consider an orthotropic functionally graded solid with primary orientation directed along the axis e_1, making an angle θ with respect to the global frame e_x, and secondary orientation e_2, which is orthogonal to e_1 as shown in Fig. 1. The boundary (Γ) is considered to admit the decomposition with the outward normal $\boldsymbol{n}$ into three disjoint sets, i.e., $\Gamma = \Gamma_D \cup \Gamma_N \cup \Gamma_c$ and $\Gamma_D \cap \Gamma_N \cap \Gamma_c = \varnothing$, where Γ_c is the crack surface, Dirichlet boundary and Neumann boundary conditions are specified on Γ_D and Γ_N respectively. The closure of the domain is $\overline{\Omega} \equiv \Omega \cup \Gamma$.

2.1. Governing equations

The spatial variation of the elastic and fracture properties inherent to functionally graded materials (FGMs) can be incorporated following the pioneering work by Hirshikesh et al. [33]. Variational phase field fracture methods are particularly suited to capture the complex crack trajectories that are observed in FGMs due to the inherent crack tip mode mixity [33,44,45]. As described below, we introduce a history field H to prevent damage irreversibility and we adopt the so-called hybrid model [46] to reduce the computational cost by keeping the linear form of the elasticity
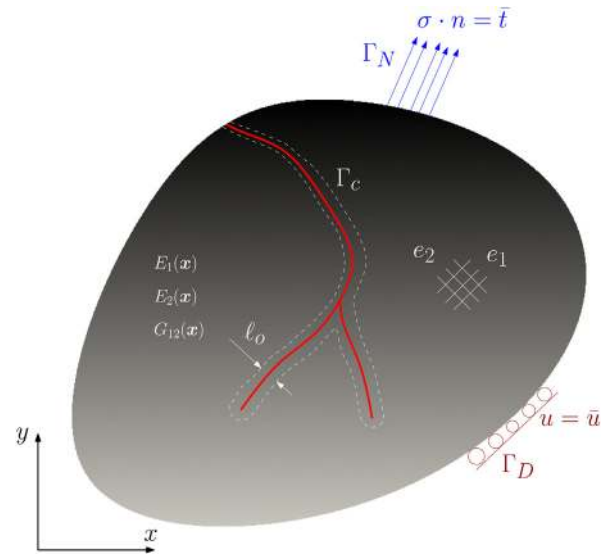

Fig. 1. Schematic representation of a orthotropic FGM domain with a geometric discontinuity in PFM framework, ℓ_o is the characteristic length scale.

equation. In addition, we decompose the strain energy density into tensile and compressive parts $\psi = \psi^+ + \psi^-$, so as to prevent damage under compressive stresses. Consider a linear elastic solid with spatially varying toughness $\mathscr{G}_c(\boldsymbol{x})$ undergoing small strains. For the displacement $\boldsymbol{u}$ and phase field ϕ, the strong form of the governing equations in the absence of inertia and body forces is given by Ref. [46,47]:

$$\nabla^e \cdot \boldsymbol{\sigma} = 0 \quad \text{in } \Omega \tag{1a}$$

$$-\mathscr{G}_c(\boldsymbol{x})\ell_o \nabla^p \phi \mathbb{A} \nabla^p \phi + \left[\frac{\mathscr{G}_c(\boldsymbol{x})}{\ell_o} + 2H^+\right]\phi = 2H^+ \quad \text{in } \Omega \tag{1b}$$

These balance equations are supplemented with the following boundary conditions:

$$\begin{aligned} \boldsymbol{\sigma} \cdot \mathbf{n} &= \overline{\boldsymbol{t}} \quad \text{on } \Gamma_N \\ \mathbf{u} &= \overline{\boldsymbol{u}} \quad \text{on } \Gamma_D \\ \nabla \phi \cdot \boldsymbol{n} &= 0 \quad \text{on } \Gamma \backslash \Gamma_c \end{aligned} \tag{2}$$

where ∇^p and ∇^e are the scalar and the vector differential operators, given by,

$$\nabla^p = \left[\frac{\partial}{\partial x} \quad \frac{\partial}{\partial y}\right]^T$$

$$\nabla^e = \begin{bmatrix} \frac{\partial}{\partial x} & 0 & \frac{\partial}{\partial y} \\ 0 & \frac{\partial}{\partial y} & \frac{\partial}{\partial x} \end{bmatrix}^T \tag{3}$$

Here $\mathbb{A} = \boldsymbol{I} + \beta[\boldsymbol{I} - \boldsymbol{n} \otimes \boldsymbol{n}]$, with $\boldsymbol{n} = \{\cos\theta, \sin\theta\}^T$ introduced to account for the crack path based on the material orientation. In this work, the penalty parameter, $\beta = 20$ is considered which constraint the propagation of crack in the direction perpendicular to the cleavage plane. The Cauchy stress tensor, $\boldsymbol{\sigma}$ for the functionally graded orthotropic material is defined as:

$$\boldsymbol{\sigma} = \left[(1 - \phi)^2 + k_p\right] \mathbb{D}(\boldsymbol{x})\boldsymbol{\varepsilon} \tag{4}$$

where k_p is a small positive number introduced for numerical

stability and

$$\mathbb{D}(\boldsymbol{x}) = \mathbb{T}^{\mathrm{T}} \boldsymbol{Q}(\boldsymbol{x}) \mathbb{T} \tag{5}$$

with

$$\mathbb{T} = \begin{bmatrix} \cos\theta & \sin\theta & 0 \\ -\sin\theta & \cos\theta & 0 \\ 0 & 0 & 1 \end{bmatrix} \tag{6}$$

and

$$\boldsymbol{Q}(\boldsymbol{x}) = \begin{bmatrix} Q_{11} & Q_{12} & 0 \\ Q_{21} & Q_{22} & 0 \\ 0 & 0 & Q_{66} \end{bmatrix} \tag{7}$$

The components of the tensor $\boldsymbol{Q}(\boldsymbol{x})$ are calculated as:

$$
\begin{aligned}
Q_{11} &= \frac{E_1(\boldsymbol{x})}{1 - \nu_{12}\nu_{21}} \\[4pt]
Q_{22} &= \frac{E_2(\boldsymbol{x})}{1 - \nu_{12}\nu_{21}} \\[4pt]
Q_{12} &= \frac{\nu_{12}E_2(\boldsymbol{x})}{1 - \nu_{12}\nu_{21}} = \frac{\nu_{21}E_1(\boldsymbol{x})}{1 - \nu_{12}\nu_{21}} \\[4pt]
Q_{66} &= G_{12}(\boldsymbol{x}) \\[4pt]
\nu_{21} &= \frac{E_2(\boldsymbol{x})}{E_1(\boldsymbol{x})}\nu_{12}
\end{aligned}
\tag{8}
$$

Here, $E_1(\boldsymbol{x})$ and $E_2(\boldsymbol{x})$ are the longitudinal and the transverse Young's modulus respectively, $G_{12}(\boldsymbol{x})$ is the shear modulus, ν_{12} is the major Poisson's ratio, and ν_{21} is the minor Poisson's ratio. Thus, material properties vary at the element level, in what is usually referred to as a *graded* finite element approach [48]. The small strain tensor ($\boldsymbol{\varepsilon}$) is computed from the displacement field ($\boldsymbol{u}$) as,

$$\boldsymbol{\varepsilon} = \frac{1}{2}\left(\nabla^e \boldsymbol{u}^{\mathrm{T}} + \nabla^e \boldsymbol{u}\right) \tag{9}$$

The history variable, H^+ is defined as,

$$H^+ := \max_{\tau \in [0,t]} \psi^+(\boldsymbol{\varepsilon}(\boldsymbol{x}, \tau)) \tag{10}$$

The introduction of H^+ in Eqn. (1b) helps to decouple Equations (1a-1b) and a robust staggered scheme can be used for computing ($\boldsymbol{u}, \phi$) [46,49]. However, one should note that monolithic quasi-Newton methods have recently shown great promise for phase field fracture problems [50,51]. Further, to prevent the crack faces from inter-penetration, Eqn. (1b) is supplemented with the following constraint:

$$\forall \boldsymbol{x} : \psi^+ < \psi^- \Rightarrow \phi := 0 \tag{11}$$

where,

$$\psi^{\pm}(\boldsymbol{\varepsilon}) = \frac{1}{2}\lambda \langle \mathrm{tr}(\boldsymbol{\varepsilon}) \rangle_{\pm}^2 + \mu \mathrm{tr}\left(\boldsymbol{\varepsilon}_{\pm}^2\right)$$

with $\langle \cdot \rangle_{\pm} := \frac{1}{2}(\cdot \pm |\cdot|)$, $\boldsymbol{\varepsilon}_{\pm} := \sum_{I=1}^{3} \langle \varepsilon_I \rangle_{\pm} \boldsymbol{n}_I \otimes \boldsymbol{n}_I$ and $\boldsymbol{\varepsilon} = \sum_{I=1}^{3} \langle \varepsilon_I \rangle \boldsymbol{n}_I \otimes \boldsymbol{n}_I$, where $\{\varepsilon_I\}_{I=1}^{3}$ and $\{\boldsymbol{n}_I\}_{I=1}^{3}$ are the principal strains and the principal strain directions, respectively.

2.2. Weak form

Let $\mathscr{W}(\Omega)$ include the linear displacement field and the phase field variable, and let $(\mathscr{U}, \mathscr{P})$ and $(\mathscr{V}, \mathscr{C})$ be the trial and the test function spaces:

$$
\begin{aligned}
\left(\mathscr{U}, \mathscr{V}^0\right) = \Big\{ &\left(\boldsymbol{u}^h, \boldsymbol{v}\right) \in \left[C^0(\Omega)\right]^d \\
&: (\boldsymbol{u}, \boldsymbol{v}) \in [\mathscr{W}(\Omega)]^d \subseteq \left[H^1(\Omega)\right]^d \Big\}
\end{aligned}
\tag{12a}
$$

$$
\begin{aligned}
\left(\mathscr{P}, \mathscr{C}^0\right) = \Big\{ &\left(\phi^h, q\right) \in \left[C^0(\Omega)\right]^d \\
&: (\phi, q) \in [\mathscr{W}(\Omega)]^d \subseteq \left[H^1(\Omega)\right]^d \Big\}
\end{aligned}
\tag{12b}
$$

Let the domain be partitioned into elements Ω^h and on using shape functions N that span at least the linear space, we substitute the trial and the test functions: $\left\{\boldsymbol{u}^h, \phi^h\right\} = \sum_I N_I \{\boldsymbol{u}_I, \phi_I\}$ and $\{\boldsymbol{v}, q\} = \sum_I N_I \{\boldsymbol{v}_I, q_I\}$ into Eqn. (13). The system of equations can be readily obtained upon applying the standard Bubnov-Galerkin procedure. Find $\boldsymbol{u}^h \in \mathscr{U}$ and $\phi^h \in \mathscr{P}$ such that, for all $\boldsymbol{v} \in \mathscr{V}^0$ and $q \in \mathscr{C}^0$,

$$\int_{\Omega} \left\{ \left[(1-\phi)^2 + k_{\mathrm{p}}\right] \boldsymbol{\sigma}(\boldsymbol{u}) : \boldsymbol{\varepsilon}(\boldsymbol{v}) \right\} d\Omega = \int_{\Gamma_t} \bar{t} \cdot \boldsymbol{v} \, d\Gamma \tag{13a}$$

$$
\begin{aligned}
\int_{\Omega} &\left[\nabla q \, \mathscr{G}_{\mathrm{c}}(\boldsymbol{x})\ell_o \, \mathbb{A} \nabla \phi + q\left(\frac{\mathscr{G}_{\mathrm{c}}(\boldsymbol{x})}{\ell_o} + 2H^+\right)\phi \right] d\Omega \\
&= \int_{\Omega} 2H^+ q \, d\Omega + \int_{\Gamma} \nabla\phi \cdot \boldsymbol{n} \, q \, d\Gamma
\end{aligned}
\tag{13b}
$$

which leads to the following system of linear equations:

$$\boldsymbol{K}^{\mathrm{uu}} \boldsymbol{u}^h = \boldsymbol{f}^{\mathrm{uu}} \tag{14a}$$

$$\boldsymbol{K}^{\phi} \phi^h = \boldsymbol{f}^{\phi} \tag{14b}$$

where

$$\boldsymbol{K}^{\mathrm{uu}} = \sum_h \int_{\Omega^h} \left[(1-\phi)^2 + k_p\right] \mathbf{B}^{\mathrm{T}} \, \mathbb{D}(\boldsymbol{x}) \, \mathbf{B} \, d\Omega, \tag{15a}$$

$$\boldsymbol{K}^{\phi} = \sum_h \int_{\Omega^h} \left[\mathbf{B}_{\phi}^{\mathrm{T}} \, \mathscr{G}_c(\boldsymbol{x})\ell_o \mathbb{A} \, \mathbf{B}_{\phi} + \mathbf{N}^{\mathrm{T}}\left(\frac{\mathscr{G}_c(\boldsymbol{x})}{\ell_o} + 2H^+\right)\mathbf{N} \right] d\Omega \tag{15b}$$

$$\boldsymbol{f}^{\mathrm{uu}} = \sum_h \int_{\Omega^h} \mathbf{N}^{\mathrm{T}} \bar{t} \, d\Omega, \tag{15c}$$

$$\boldsymbol{f}^{\phi} = \sum_h \int_{\Omega^h} \mathbf{N}^{\mathrm{T}} 2H^+ \, d\Omega, \tag{15d}$$

Here, $\boldsymbol{B} = \nabla^e \boldsymbol{N}$ is the strain-displacement matrix and $\boldsymbol{B}_{\phi} = \nabla^p \boldsymbol{N}$ is the scalar gradient of the shape function matrix $\boldsymbol{N}$. The above system of equations are solved by the staggered approach [46,49]. The present framework is implemented in Matlab. The reader is referred to Ref. [52] for a FEniCS-based implementation, Ref. [53]
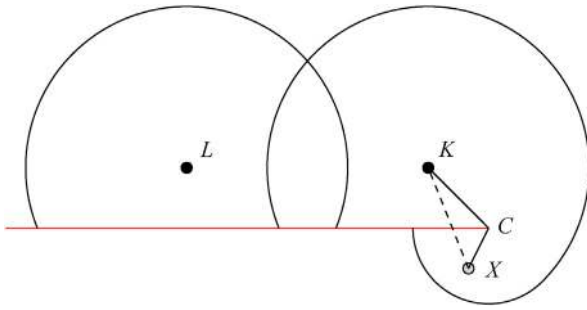
Fig. 2. Diffraction method for calculating weight function considering discontinuities in moving least-squares approximations (red line shows the discontinuity).

for a COMSOL-based implementation, Ref. [54] for an Abaqus-based implementation, and to Ref. [43] for machine learning solution scheme.

3. Recovery based error indicator and quadtree decomposition

In this section, we present a brief overview of the recovery based error indicator proposed by Bordas and Duflot [55,56] for the XFEM. This is done to assess the error and identify the elements/regions which have to be refined. Later, the process of quadtree decomposition is discussed.

3.1. Recovery based error indicator

In this method, the enhanced strain field is computed using the standard nodal solution through the eXtended Moving Least Square (XMLS) derivative recovery process. This is then further used as error indicator. Let $\boldsymbol{x}$ be a point in the domain, and n_x XMLS points contain $\boldsymbol{x}$ in their domain of influence. Then, using the displacement values at these n_x points, the enhanced displacement field and the strain field at $\boldsymbol{x}$ can be written as,

$$\boldsymbol{u}^s(\mathbf{x}) = \sum_{I=1}^{n_x} \psi_k(\boldsymbol{x}) \boldsymbol{u}_k^h = \boldsymbol{\Psi}^{\mathrm{T}}(\boldsymbol{x}) \boldsymbol{u}^h \tag{16}$$

$$\boldsymbol{\varepsilon}^s(\boldsymbol{x}) = \sum_{I=1}^{n_x} \mathscr{D}(\psi_k)(\boldsymbol{x}) \boldsymbol{u}_k^h = \boldsymbol{D}(\boldsymbol{x}) \boldsymbol{u}^h \tag{17}$$

where $\Psi_k(x)$ is the MLS shape function value associated with node k at $\boldsymbol{x}$, $\mathscr{D}$ is the derivative operator and D is the MLS shape function derivative matrix. The matrix form of the MLS shape function is given by:

$$\boldsymbol{\Psi}^{\mathrm{T}}(\boldsymbol{x}) = [\psi_1(\boldsymbol{x}) \psi_2(\boldsymbol{x}) \dots \psi_{n_x}(\boldsymbol{x})] = \boldsymbol{p}^{\mathrm{T}}(\boldsymbol{x}) \boldsymbol{A}^{-1}(\boldsymbol{x}) \boldsymbol{B}(\boldsymbol{x}) \tag{18}$$

where $\boldsymbol{p}(\boldsymbol{x})$ denotes the m reproducing polynomial used for the MLS shape function. For two dimensions, $\boldsymbol{p}(\boldsymbol{x}) = [1 \quad x \quad y]$, and,

$$w_1(\mathbf{x})\mathbf{p}(\mathbf{x}_1) w_2(\mathbf{x})\mathbf{p}(\mathbf{x}_2) \dots w_{n_x}(\mathbf{x})\mathbf{p}(\mathbf{x}_{n_x})$$

Here, $\boldsymbol{A}$ is a $m \times m$ matrix and $\boldsymbol{B}$ is a $m \times n_x$ matrix. For the matrix $\boldsymbol{A}$ to be invertible, we need $n_x > m$, i.e., we need more number of points whose domains of influence contains x that the basis functions in $\boldsymbol{p}$. However, note that this is not a sufficient condition. The weight function $\boldsymbol{w}_I$ associated with a node $\boldsymbol{x}_I$ is calculated by the diffraction method with a circular domain of influence. The domain of influence also changes if it intersects with the discontinuity. In this work, a fourth order spline is taken as the weighting function [56]:

$$w_k(\boldsymbol{x}) = \begin{cases} 1 - 6s^2 + 8s^3 - 3s^4 & \text{if } |s| \leq 1 \\ 0 & \text{if } |s| > 1 \end{cases} \tag{19}$$

where $s = \frac{||\boldsymbol{x} - \boldsymbol{x}_k||}{d_k}$ and d_k denotes the support domain of node $\boldsymbol{x}_k$. s is calculated differently than above to account for a discontinuity in the approximation. When describing a discontinuity, if it covers a point, a node's weight at this point will decrease. When the line section $C_i X$ of Fig. 2 is bisected by a crack, s of Eq. (19) is substituted by the normalized length of the shortest path from K to X that passes through a front point (route KCX in Fig. 2).

$$s = \frac{||\boldsymbol{x} - \boldsymbol{x}_c|| + \boldsymbol{x}_c - \boldsymbol{x}_k}{d_k} \tag{20}$$

The enhanced derivatives of the shape functions are computed by finding the derivatives of the MLS shape functions, see Eqn. (18). The enhanced derivatives of the displacements and the enhanced small strain $\boldsymbol{\varepsilon}_s$ can then be found. The error is computed by comparing the enhanced strain field to the standard compatible
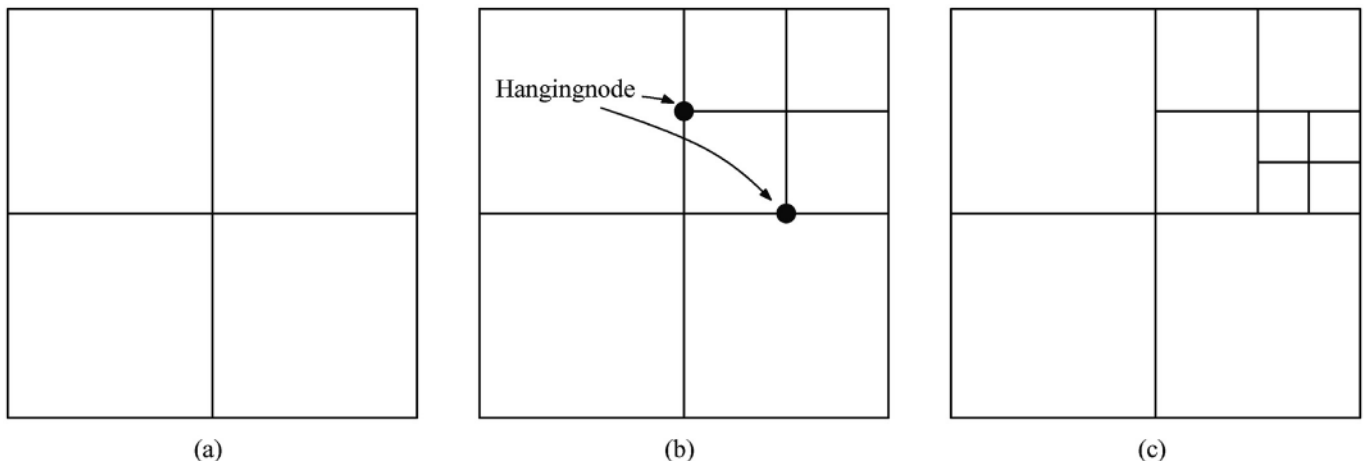

Fig. 3. Quadtree decomposition: (a) representative quadtree mesh and (b) tree structure employed to store the mesh details.

strain field. Thus, the total error of domain Ω is,

$$||\boldsymbol{e}||_\Omega = \sqrt{\int_\Omega ||\boldsymbol{\varepsilon}(\boldsymbol{x}) - \boldsymbol{\varepsilon}_s(\boldsymbol{x})||^2 \, d\boldsymbol{x}} \qquad (21)$$

while the error within the element i with area Ω_i is,

$$||\boldsymbol{e}||_{\Omega_i} = \sqrt{\int_{\Omega i} \boldsymbol{\varepsilon}(\boldsymbol{x}) - \boldsymbol{\varepsilon}_s(\boldsymbol{x})^2 \, d\boldsymbol{x}} \qquad (22)$$

The tolerance is chosen based on the maximum error criteria. Thus, the elements with high individual error are discretized in the next level; all elements whose individual error is higher than given tolerance value will be sent for discretization in the next level.

3.2. Quadtree decomposition

The quadtree decomposition is used for local refinement once the error is quantified. The quadtree decomposition entails several features; namely, (a) is easy to implement (b) it requires less degrees of freedom (Dofs) and (c) retains hierarchical mesh
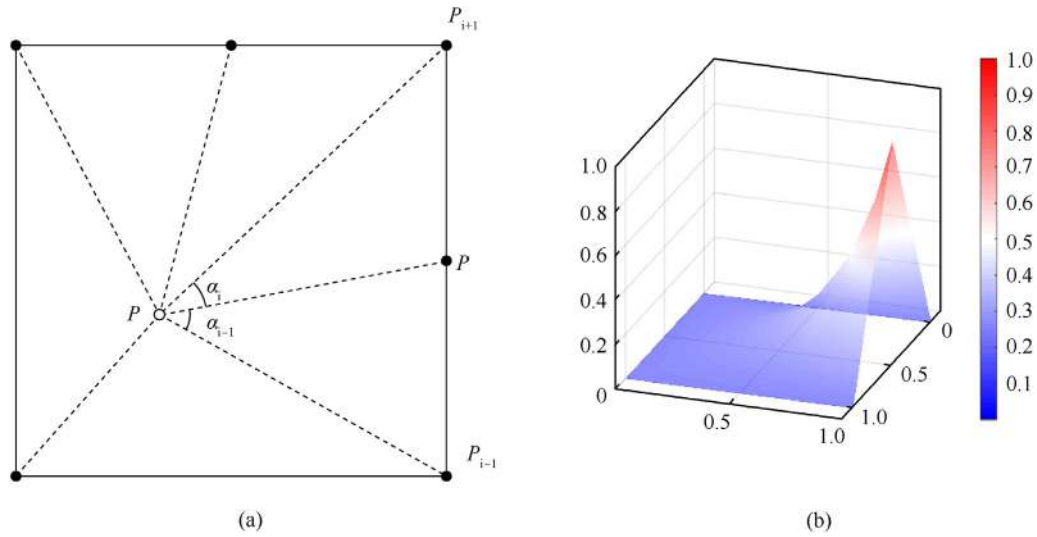

Fig. 4. Schematic representation of an element with hanging node and the construction of mean value shape function.
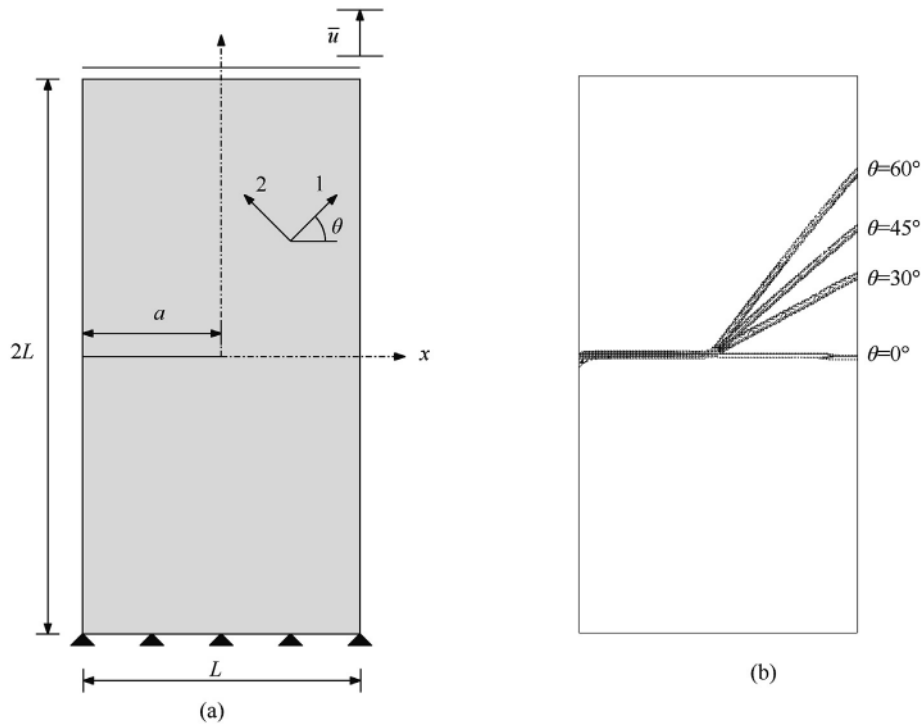

Fig. 5. Edge crack orthotropic specimen: (a) geometry, material properties and boundary conditions (b) crack propagation direction for different material orientation. [where $L = 1$ mm and $a = 0.5$ mm].

structures. The hierarchical mesh structure facilitates efficient computations, particularly efficient storage and data retrieval. In this decomposition, the so-called stopping criterion is used to decide which element requires to be further refined. This criterion can be a geometry based factor or any error indicator. The criteria for an element to be refined based on the error indicator could be based on either equal distribution criterion or Min-number criteria [57]. In this work, equal distribution criterion is used to minimize
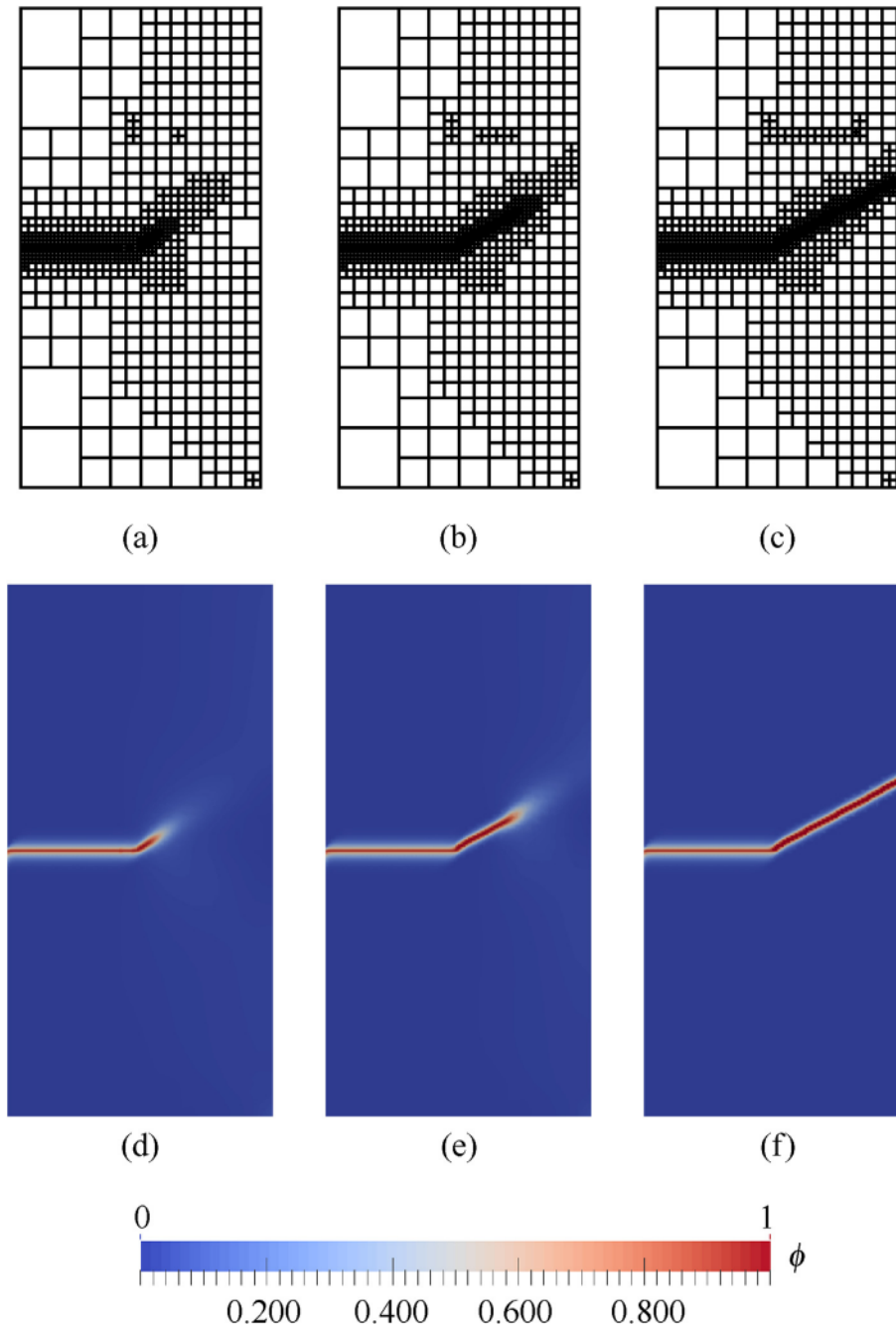
Fig. 6. Domain discretization of edge crack specimen with $\theta = 30°$ at (a) 0.035 (b) 0.038 and (c) 0.039 mm.

Table 1
Computational time (in seconds) comparison for adaptive PFM and PFM with uniform refinement.

PFM strategy	DOFs	computation times (sec)					
		Error indicator	remeshing	assemble (ϕ)	soln (ϕ)	assembly ($\boldsymbol{u}$)	soln ($\boldsymbol{u}$)
Adaptive refinement	2772	4.2	0.74	0.48	0.004	0.62	0.012
Uniform refinement	108,336	—	—	11.3	0.30	17.04	1.48

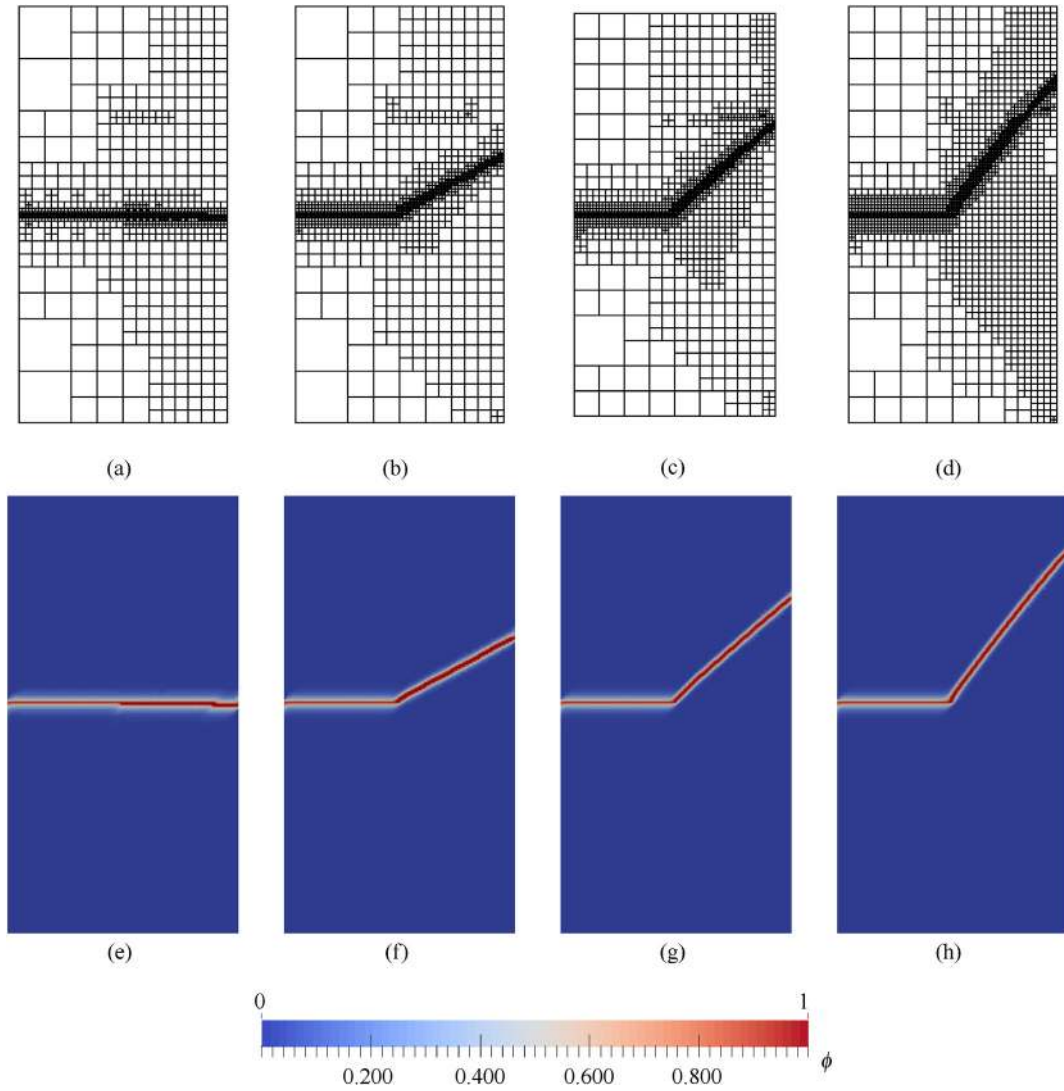**Fig. 7.** Final domain discretization for (a) $\theta = 0°$ (b) $\theta = 30°$ (c) $\theta = 45°$ and (d) $\theta = 60°$ and the corresponding crack trajectory in (e,f,g,h), respectively.
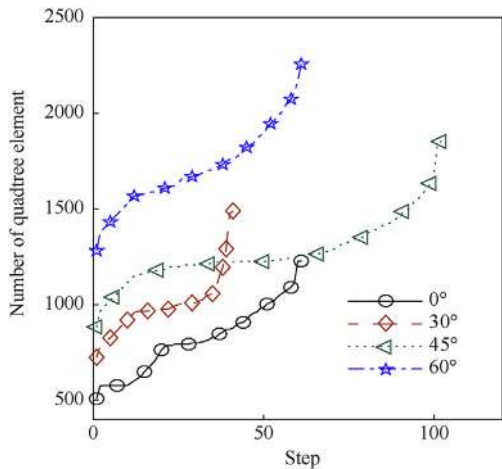

Fig. 8. Quadtree evolution as a function of load step.

Table 2
Crack propagation angle compared with the experiments and the XFEM.

Fiber Orientation (degree)	0∘	30∘	45∘	60∘
θ_{inc} Experimental [64]	0	30	45	60
θ_{inc} XFEM [64]	0	29	43	57
θ_{inc} present PFM	0	29.1	43	55

the global error and balance the local error throughout the domain. If the given element does not satisfy the stopping criterion within the user specified tolerance limit, it will be divided into four child elements as shown in Fig. 3. This process can be repeated several times until the criteria is met. The tolerance in all the examples is chosen to be 1×10^{-5}.

The aforementioned decomposition leads to elements with hanging nodes; see, Fig. 3. The conventional finite element approach cannot handle such elements without additional work. This is because of lack of compatibility between the elements. To

restrict the number of hanging nodes per edge, a general practice 2:1 rule is applied, in which the mesh is constructed in such a way that two neighboring elements do not differ by more than one level. A number of techniques to handle these hanging nodes have been proposed, such as triangulation [58], transformation of the hanging degrees of freedom to corner degrees of freedom using constraint equations [59], use of special conforming shape functions [60], considering the element with hanging nodes as a polygon [61], or the use of other advanced methods like Scaled Boundary Finite Element Method (SBFEM) or Smoothed Finite Element Method (SFEM) [62].

In this work, the elements with hanging nodes are considered as *n*-sided polygons (see Fig. 4a). The mean - value shape functions proposed by Floater [63] are used to approximate the unknown fields. The reasons behind this choice are the facts that some angles of elements with hanging nodes are 180° and the mean value shape-functions work efficiently for non-convex polygons.

The mean - value coordinates for a point $P(\boldsymbol{x})$ in an arbitrary polygon are given by:

$$N_i(\boldsymbol{x}) = \frac{\omega_i(\boldsymbol{x})}{\sum_{j=1}^{n} \omega_i(\boldsymbol{x})}, \quad i = 1, \cdots, n$$

$$\omega_i(\boldsymbol{x}) = \frac{\tan(\alpha_{i-1}/2) + \tan(\alpha_i/2)}{\boldsymbol{x} - \boldsymbol{x}_i}$$

(23)

where n is the number of nodes in an element, $\boldsymbol{x}_i$ are the co-ordinates of point P_i and α_i's are the internal angles. Fig. 4b shows the mean value shape function for the polygon with hanging node. The numerical integration for the polygonal elements is performed by subdividing the polygon into triangles and employing standard quadrature rule.

4. Results

In this section, the performance and the robustness of the adaptive PFM for fracture of orthotropic FGMs is investigated. We first validate the adaptive PFM results against experimental and numerical results for failure of orthotropic materials. Then, cracking of orthotropic FGMs is investigated for different material grading possibilities. The numerical stability parameter k_p is assumed to be 1×10^{-6} in all the numerical examples, unless specified otherwise. The proposed adaptive PFM is implemented in MATLAB R2014b and the simulations were performed on Intel quad Core i5-4590CPU@3.30 GHz with 8 GiB RAM.

4.1. Validation: fracture of orthotropic materials

The framework developed is validated first with the experimental and numerical work (XFEM) of Cahill et al., [64]. In order to study the fracture processes in an orthotropic material, an edge crack specimen subjected to tensile loading is considered, see Fig. 5a. The material properties are chosen as: $E_1 = 114.8$ GPa, $E_2 = 11.7$ GPa, $G_{12} = 9.66$ GPa, $\nu_{12} = 0.21$ and the critical toughness $\mathscr{G}_c = 2.7$ MPa mm.

The simulation starts with a coarse mesh and an assumed characteristic length scale, ℓ_o. For each load step, the domain is discretized as explained in Section 3, which allows to track the crack trajectory continuously. Fig. 6 shows the domain discretization for the evolving crack trajectory; the combination of quadtree decomposition and post-errori error estimator strategies leads to a fine discretization in the vicinity of the propagating crack tip. This feature substantially reduces the size of the global stiffness matrix, resulting in reduced CPU memory requirement and efficient computations.

We proceed to quantify the computational gains by comparing to the case of uniform refinement. Computation times are compared to those obtained from a solution with uniform mesh, where the characteristic element size equals the element size in the crack region in the adaptive re-meshing case. Results are shown in Table 1 for the initial load step Δu, after convergence has been achieved. The number of degrees of freedom (DOFs) is also shown.
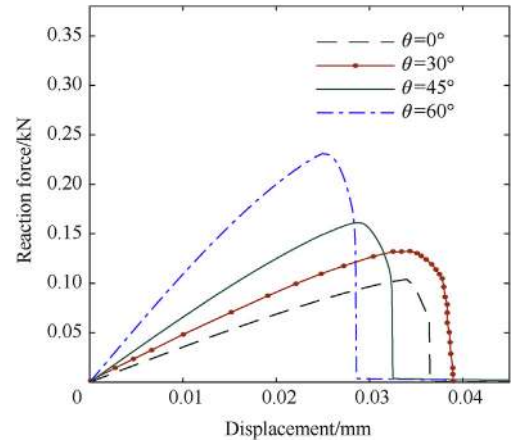
Fig. 9. Load displacement response for the orthotropic material with different material orientation, θ.
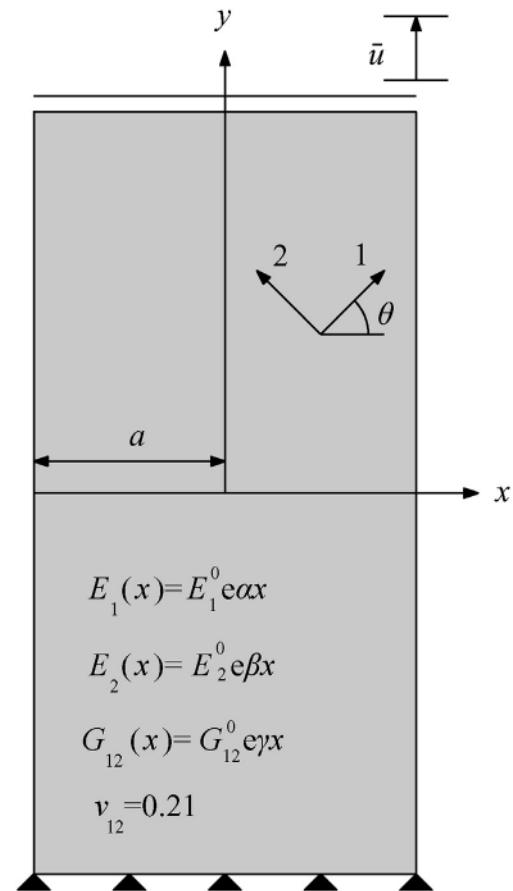
Fig. 10. Orthotropic FGM specimen: domain and boundary conditions, (α, β, γ) are indices that control the material variation.

Very substantial computationally gains are reported relative to the uniform mesh scenario, due to the significantly smaller number of DOFs required when using an adaptive mesh refinement strategy. The error indicator is the most time consuming operation in the adaptive PFM.

Fig. 5b shows the crack propagation trajectory for four selected values of material orientation i.e., $\theta = 0°, 30°, 45°, 60°$. The corresponding domain discretization is shown in Fig. 7. In agreement with expectations, the crack propagation path strictly follows the material orientations, see Fig. 5b.

Fig. 8 shows how the number of quadtree elements increases as the crack propagates. It is shown that the material orientation angles that translate into a larger crack deflection require a larger number of quadtree elements. The comparison with the results obtained in experiments and XFEM-based calculations [64] are shown in Table 2. A very good agreement is attained for all values of material orientation.

Finally, Fig. 9 shows the load-displacement response of the orthotropic specimen with different material orientations. The stiffness of the response increases with the material orientation angle θ.

4.2. Fracture of orthotropic functionally graded materials

Next, we examine the fracture processes in an orthotropic FGM specimen as shown in Fig. 10. In terms of material gradation, we consider the following representative case studies:

- plate with a crack parallel to the material gradation i.e., $x-$ direction grading,
- plate with a crack perpendicular to the material gradation i.e., $y-$ direction grading.

For simplicity, we assume that the material property variation follows an exponential gradation, as characterized by the indices α, β, γ - see Fig. 10. As shown in Fig. 11, two different scenarios have been considered: (i) proportional and (ii) non-proportional gradation strategies, in terms of the material indices. In the former, the indices, α, β, γ are set to 0.2, whilst for non-proportional variation, we choose, $(\alpha, \beta, \gamma) = (0.5, 0.4, 0.3)$. The material constants are
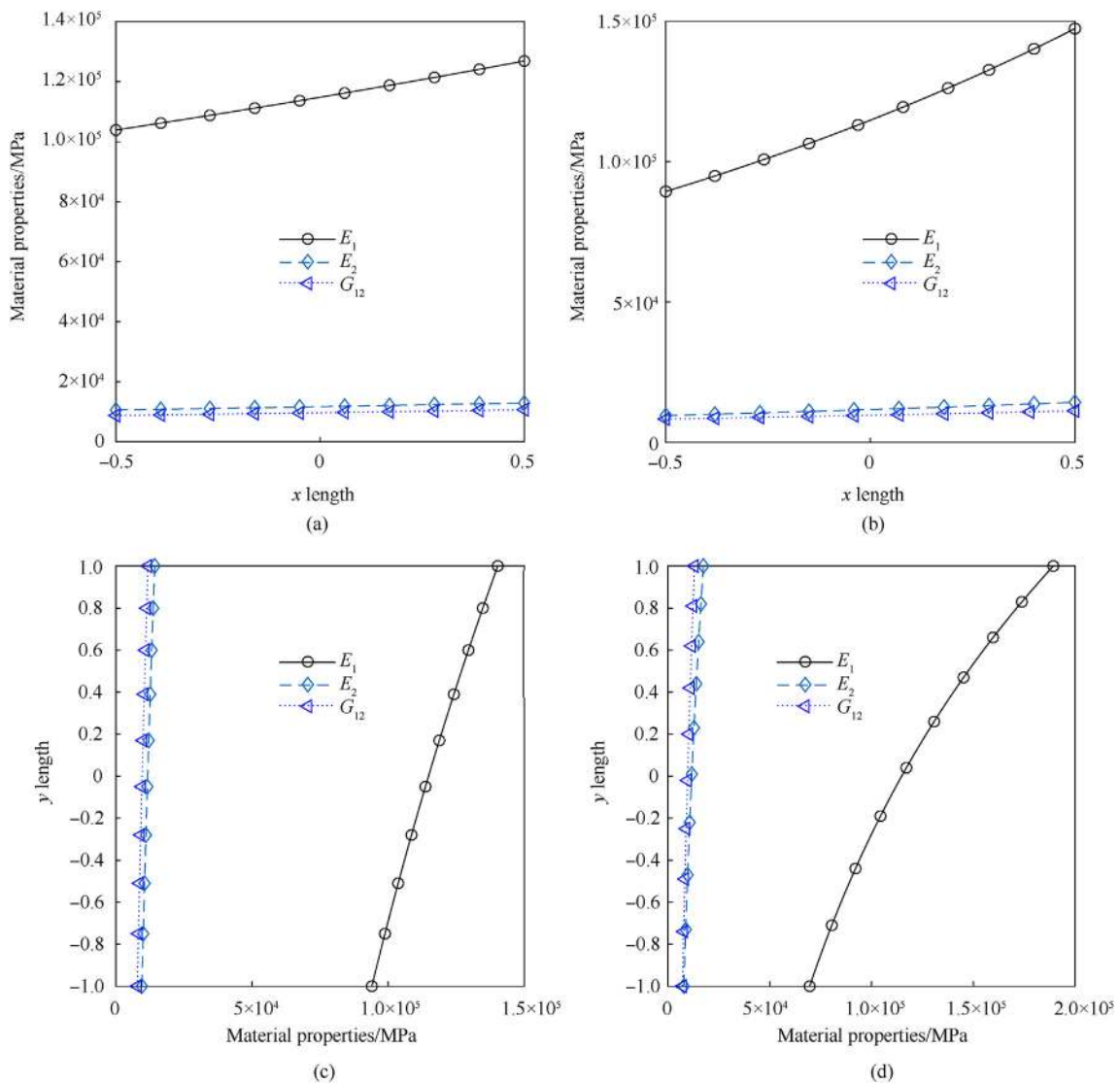

Fig. 11. FGM orthotropic material gradation in (a) $x-$ direction with proportional material gradation (b) $x-$ direction with non-proportional material gradation (c) $x-$ direction with proportional material gradation, and (d) $y-$ direction with non-proportional material gradation.
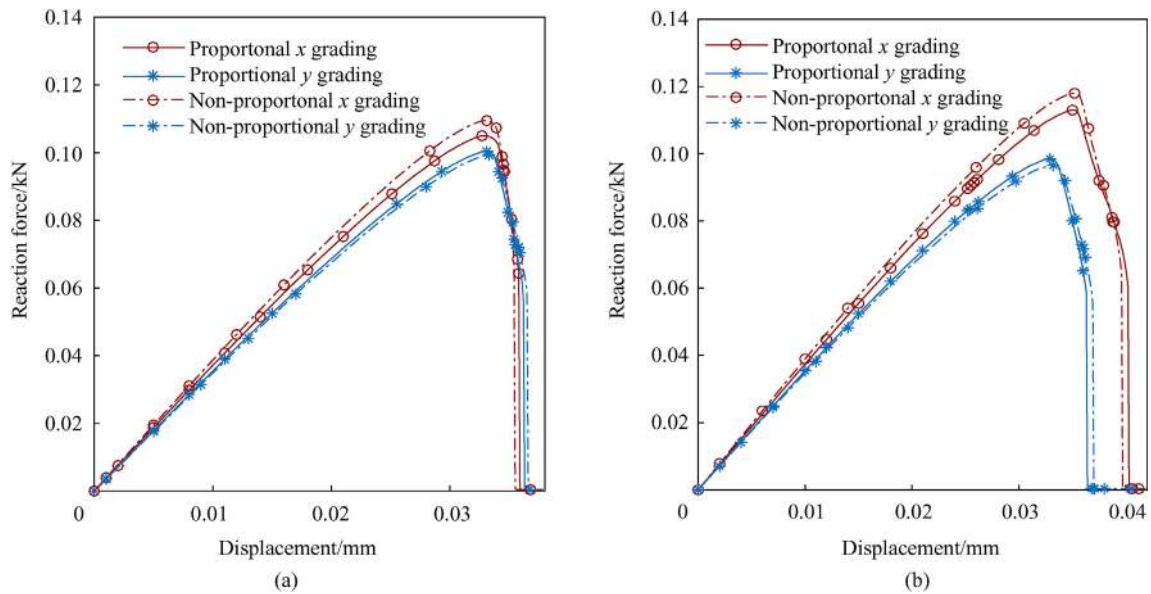
Fig. 12. Load-displacement response for FGM orthotropic specimen with (a) with constant toughness $\mathscr{G}_c$, and (b) with varying toughness $\mathscr{G}_c(\boldsymbol{x})$.

chosen as: $E_1^0 = 114.8$ GPa, $E_2^0 = 11.7$ GPa, $G_{12}^0 = 9.66$ GPa, and the critical toughness $\mathscr{G}_c = 2.7$ MPa mm. With respect to the critical energy release rate $\mathscr{G}_c$, two cases are considered; one, where no material gradation is assumed and a graded one that follows the material gradation depicted in Fig. 10. For all results, the orthotropic material orientation is take to be $\theta = 0°$.

In all cases, given that the same value of θ is considered, the predicted crack trajectories follow an almost identical path. However, differences can be seen in the load-displacement curves, as shown in Fig. 12. Consider first the effect of a proportional or non-proportional material gradation, the same qualitative trends are seen in both Fig. 12a and b. For the case of material gradation in $x-$ direction, the non-proportional material gradation shows stiffer response than the proportional material gradation. This trend is reversed for the case of material gradation in $y-$ direction, where differences are minimal. Differences are due to the crack tip non-homogeneity, which affects the mode mixity. Consider now the influence of spatially varying the material critical energy release rate $\mathscr{G}_c$ toughness, i.e. Fig. 12a versus Fig. 12b. It can be seen that differences are substantial in the case of material grading along the x-direction. In agreement with expectations, the propagating crack encounters an increasing resistance to fracture as the magnitude of $\mathscr{G}_c$ at the crack tip raises with crack advance.

5. Conclusions

We have presented a novel framework for modelling fracture problems in orthotropic functionally graded materials (FGMs). The framework builds upon the phase field fracture method for FGMs and an adaptive mesh technique based on a recovery based error indicator and quadtree decomposition. Results show the capability of the model in capturing complex crack trajectories, not known a priori, while minimising the computational cost. The numerical framework is validated by comparing to experimental and numerical results on non-graded orthotropic materials. A good agreement is observed. Then, calculations are shown for orthotropic FGMs and the role of the material gradation indeces explored. Topics of interest for future work involve extending the present framework to dynamic crack growth, three dimensions problems and enabling mesh coarsening behind the crack.

References

[1] Aboudi J, Arnold SM, Pindera MJ. Response of functionally graded composites to thermal gradients. Compos Eng 1994;4(1):1—18.
[2] Pindera M-J, Aboudi J, Arnold SM. Thermomechanical analysis of functionally graded thermal barrier coatings with different microstructural scales. J Am Ceram Soc 1998;36(6):1525—36.
[3] Lee YD, Erdogan F. Residual/thermal stresses in FGM and laminated thermal barrier coatings. Int J Fract 1994;69(2):145—65.
[4] Ramaswamy P, Seetharamu S, Varma K, Rao K. Al2O3-ZrO2 Composite coatings for thermal-barrier applications. Compos Sci Technol 1997;57:81—9.
[5] Tilbrook MT, Rozenburg K, Steffler ED, Rutgers L, Hoffman M. Crack propagation paths in layered, graded composites. Compos B Eng 2006;37(6):490—8.
[6] Uemura S. The activities of FGM on new application. Mater Sci Forum 2003;423—425:1—10.
[7] Martínez-Pañeda E, Gallego R. Numerical analysis of quasi-static fracture in functionally graded materials. Int J Mech Mater Des 2015;11(4):405—24.
[8] Kim J-H, Paulino GH. Mixed-mode fracture of orthotropic functionally graded materials using finite elements and the modified crack closure method. Eng Fract Mech 2002;69(14):1557—86.
[9] Kim J-H, Paulino GH. T-stress in orthotropic functionally graded materials: Lekhnitskii and stroh formalisms. Int J Fract 2004;126(4):345—84.
[10] Hosseini S, Bayesteh H, Mohammadi S. Thermo-mechanical XFEM crack propagation analysis of functionally graded materials. Mater Sci Eng, A 2013;561:285—302.
[11] Bayesteh H, Mohammadi S. XFEM fracture analysis of orthotropic functionally graded materials. Compos B Eng 2013;44(1):8—25.
[12] Chen X, Luo T, Ooi E, Ooi E, Song C. A quadtree-polygon-based scaled boundary finite element method for crack propagation modeling in functionally graded materials. Theor Appl Fract Mech 2018;94:120—33.
[13] Ooi ET, Song C, Natarajan S. A scaled boundary finite element formulation with bubble functions for elasto-static analyses of functionally graded materials. Comput Mech 2017;60:943—67.
[14] Goli E, Bayesteh H, Mohammadi S. Mixed mode fracture analysis of adiabatic cracks in homogeneous and non-homogeneous materials in the framework of partition of unity and the path-independent interaction integral. Eng Fract

Mech 2014;131:100—27.

[15] Yildirim B, Yilmaz S, Kadioglu S. Delamination of compressively stressed orthotropic functionally graded material coatings under thermal loading. J Appl Mech 2008;75(5):51106—16.

[16] Bouchard P, Bay F, Chastel Y. Numerical modelling of crack propagation: automatic remeshing and comparison of different criteria. Comput Methods Appl Mech Eng 2003;192(35):3887—908.

[17] Francfort G, Marigo J-J. Revisiting brittle fracture as an energy minimization problem. J Mech Phys Solid 1998;46(8):1319—42.

[18] Bourdin B, Francfort GA, Marigo JJ. The variational approach to fracture. Springer Netherlands; 2008.

[19] McAuliffe C, Waisman H. A coupled phase field shear band model for ductile-brittle transition in notched plate impacts. Comput Methods Appl Mech Eng 2016;305:173—95.

[20] Bleyer J, Alessi R. Phase-field modeling of anisotropic brittle fracture including several damage mechanisms. Comput Methods Appl Mech Eng 2018;336: 213—36.

[21] Zhou S, Zhuang X, Rabczuk T. Phase field modeling of brittle compressive-shear fractures in rock-like materials: a new driving force and a hybrid formulation. Comput Methods Appl Mech Eng 2019;355:729—52.

[22] Borden MJ, Hughes TJR, Landis CM, Anvari A, Lee IJ. A phase-field formulation for fracture in ductile materials: finite deformation balance law derivation, plastic degradation, and stress triaxiality effects. Comput Methods Appl Mech Eng 2016;312:130—66.

[23] Miehe C, Aldakheel F, Raina A. Phase field modeling of ductile fracture at finite strains: a variational gradient-extended plasticity-damage theory. Int J Plast 2016;84:1—32.

[24] Ren H, Zhuang X, Anitescu C, Rabczuk T. An explicit phase field method for brittle dynamic fracture. Comput Struct 2019;217:45—56.

[25] Msekh MA, Cuong N, Zi G, Areias P, Zhuang X, Rabczuk T. Fracture properties prediction of clay/epoxy nanocomposites with interphase zones using a phase field model. Eng Fract Mech 2018;188:287—99.

[26] Reinoso J, Paggi M, Linder C. Phase field modeling of brittle fracture for enhanced assumed strain shells at large deformations: formulation and finite element implementation. Comput Mech 2017;59(6):981—1001.

[27] Carollo V, Reinoso J, Paggi M. A 3D finite strain model for intralayer and interlayer crack simulation coupling the phase field approach and cohesive zone model. Compos Struct 2017;182:636—51.

[28] Hirshikesh, Natarajan S, Annabattula RK. Modeling crack propagation in variable stiffness composite laminates using the phase field method. Compos Struct 2019;209:424—33.

[29] Amiri F, Millán D, Shen Y, Rabczuk T, Arroyo M. Phase-field modeling of fracture in linear thin shells. Theor Appl Fract Mech 2014;69:102—9.

[30] Areias P, Rabczuk T, Msekh M. Phase-field analysis of finite-strain plates and shells including element subdivision. Comput Methods Appl Mech Eng 2016;312:322—50.

[31] Martínez-Pañeda E, Golahmar A, Niordson CF. A phase field formulation for hydrogen assisted cracking. Comput Methods Appl Mech Eng 2018;342: 742—61.

[32] Martinez-Pañeda E, Harris ZD, Fuentes-Alonso S, Scully JR, Burns JT. On the suitability of slow strain rate tensile testing for assessing hydrogen embrittlement susceptibility. Corrosion Sci 2020;163:108291.

[33] Hirshikesh, Natarajan S, Annabattula RK, Martínez-Pañeda E. Phase field modelling of crack propagation in functionally graded materials. Compos B Eng 2019;169:239—48.

[34] Patil R, Mishra B, Singh I. An adaptive multiscale phase field method for brittle fracture. Comput Methods Appl Mech Eng 2018;329:254—88.

[35] Tian F, Tang X, Xu T, Yang J, Li L. A hybrid adaptive finite element phase-field method for quasi-static and dynamic brittle fracture. Int J Numer Methods Eng 2019;120(9):1108—25.

[36] Mang K, Walloth M, Wick T, Wollner W. Mesh adaptivity for quasi-static phase-field fractures based on a residual-type a posteriori error estimator. GAMM-Mitteilungen; 2019, e202000003.

[37] Hirshikesh, Jansari C, Kannan K, Annabattula R, Natarajan S. Adaptive phase field method for quasi-static brittle fracture using a recovery based error indicator and quadtree decomposition. Eng Fract Mech 2019;220:106599.

[38] Mahnken R. Goal-oriented adaptive refinement for phase field modeling with finite elements. Int J Numer Methods Eng 2013;94(4):418—40.

[39] Hirshikesh, Pramod A, Annabattula R, Ooi E, Song C, Natarajan S. Adaptive phase-field modeling of brittle fracture using the scaled boundary finite

[40] Areias P, Reinoso J, Camanho P, de Sá JC, Rabczuk T. Effective 2D and 3D crack propagation with local mesh refinement and the screened Poisson equation. Eng Fract Mech 2018;189:339—60.

[41] Areias P, Msekh M, Rabczuk T. Damage and fracture algorithm using the screened Poisson equation and local remeshing. Eng Fract Mech 2016;158(Supplement C):116—43.

[42] Goswami S, Anitescu C, Rabczuk T. Adaptive fourth-order phase field analysis for brittle fracture. Comput Methods Appl Mech Eng 2020;361:112808.

[43] Samaniego E, Anitescu C, Goswami S, Nguyen-Thanh VM, Guo H, Hamdia K, Zhuand X, Rabczuk T. An energy approach to the solution of partial differential equations in computational mechanics via machine learning: concepts,implementation and applications. Comput Methods Appl Mech Eng 2020;362:112790.

[44] Doan DH, Bui TQ, Duc ND, Fushinobu K. Hybrid phase field simulation of dynamic crack propagation in functionally graded glass-filled epoxy. Compos B Eng 2016;99:266—76.

[45] Van Do T, Doan DH, Duc ND, Bui TQ. Phase-field thermal buckling analysis for cracked functionally graded composite plates considering neutral surface. Compos Struct 2017;182:542—8.

[46] Ambati M, Gerasimov T, De Lorenzis L. A review on phase-field models of brittle fracture and a new fast hybrid formulation. Comput Mech 2015;55: 383—405.

[47] Nguyen TT, Réthoré J, Baietto M-C. Phase field modelling of anisotropic crack propagation. Eur J Mech Solid 2017;65:279—88.

[48] Martínez-Pañeda E. On the finite element implementation of functionally graded materials. Materials 2019;12:287.

[49] Miehe C, Hofacker M, Welschinger F. A phase field model for rate-independent crack propagation: robust algorithmic implementation based on operator splits. Comput Methods Appl Mech Eng 2010;199(45):2765—78.

[50] Wu J-Y, Huang Y, Nguyen VP. On the BFGS monolithic algorithm for the unified phase field damage theory. Comput Methods Appl Mech Eng 2020;360.

[51] Kristensen PK, Martínez-Pañeda E. Phase field fracture modelling using quasi-Newton methods and a new adaptive step scheme. In: Theoretical and Applied Fracture Mechanics, 107; 2020. p. 102446.

[52] Hirshikesh, Natarajan S, Annabattula RK. A FEniCS implementation of the phase field method for quasi-static brittle fracture. Front Struct Civ Eng 2019;13(2):380—96.

[53] Zhou S, Rabczuk T, Zhuang X. Phase field modeling of quasi-static and dynamic crack propagation: comsol implementation and case studies. Adv Eng Software 2018;122:31—49.

[54] Msekh MA, Sargado JM, Jamshidian M, Areias PM, Rabczuk T. Abaqus implementation of phase-field model for brittle fracture. Comput Mater Sci 2015;96(PB):472—84.

[55] Bordas S, Nguyen PV, Dunant C, Guidoum A, Nguyen-Dang H. An extended finite element library. Int J Numer Methods Eng 2007;71(6):703—32.

[56] Bordas SPA, Duflot M, Le P. A simple error estimator for extended finite elements. Commun Numer Methods Eng 2008;24(11):961—71.

[57] Jin Y, González-Estrada O, Pierard O, Bordas S. Error-controlled adaptive extended finite element method for 3D linear elastic crack propagation. Comput Methods Appl Mech Eng 2017;318:319—48.

[58] Greaves DM, Borthwick AGL. Hierarchical tree-based finite element mesh generation. Int J Numer Methods Eng 1999;45(4):447—71.

[59] Fries TP, Byfut A, Alizada A, Cheng KW, Schröder A. Hanging nodes and XFEM. Int J Numer Methods Eng 2011;86(4—5):404—30.

[60] Gupta AK. A finite element for transition from a fine to a coarse grid. Int J Numer Methods Eng 1978;12(1):35—45.

[61] Tabarraei A, Sukumar N. Adaptive computations on conforming quadtree meshes. Finite Elem Anal Des 2005;41(7):686—702.

[62] Natarajan S, Ooi ET, Song C. Finite element computations over quadtree meshes: strain smoothing and semi-analytical formulation. Int. J. Adv. Eng. Sci. Appl. Math. 2015;7(3):124—33.

[63] Floater MS. Mean value coordinates. Comput Aided Geomet Des 2003;20(1): 19—27.

[64] Cahill L, Natarajan S, Bordas S, O'Higgins R, McCarthy C. An Experimental/ Numerical investigation in to the main driving force for crack propagation in uni-directional fibre-reinforced composite laminae. Compos Struct 2013;107: 119—30.